

# Dynamic Behavior of CuZn Nanoparticles under Oxidizing and Reducing Conditions

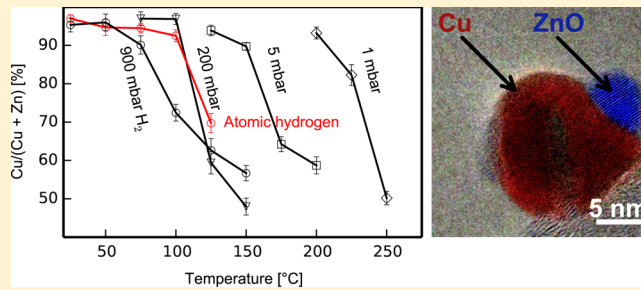
Christian Holse,<sup>†</sup> Christian F. Elkjær,<sup>†,‡</sup> Anders Nierhoff,<sup>†</sup> Jens Sehested,<sup>‡</sup> Ib Chorkendorff,<sup>†</sup> Stig Helveg,<sup>\*,‡</sup> and Jane H. Nielsen<sup>\*,†</sup>

<sup>†</sup>Center for Individual Nanoparticle Functionality, Department of Physics, Technical University of Denmark, DK-2800 Kongens Lyngby, Denmark

<sup>‡</sup>Haldor Topsoe A/S, Nymøllevej 55, DK-2800 Kongens Lyngby, Denmark

## Supporting Information

**ABSTRACT:** The oxidation and reduction of CuZn nanoparticles was studied using X-ray photoelectron spectroscopy (XPS) and in situ transmission electron microscopy (TEM). CuZn nanoparticles with a narrow size distribution were produced with a gas-aggregation cluster source in conjunction with mass-filtration. A direct comparison between the spatially averaged XPS information and the local TEM observations was thus made possible. Upon oxidation in O<sub>2</sub>, the as-deposited metal clusters transform into a polycrystalline cluster consisting of separate CuO and ZnO nanocrystals. Specifically, the CuO is observed to segregate to the cluster surface and partially cover the ZnO nanocrystals. Upon subsequent reduction in H<sub>2</sub> the CuO converts into metallic Cu with ZnO nanocrystal covering their surface. In addition, a small amount of metallic Zn is detected suggesting that ZnO is reduced. It is likely that Zn species can migrate to the Cu surface forming a Cu–Zn surface alloy. The oxidation and reduction dynamics of the CuZn nanoparticles is of great importance to industrial methanol synthesis for which the direct interaction of Cu and ZnO nanocrystals synergistically boosts the catalytic activity. Thus, the present results demonstrate a new model approach that should be generally applicable to address metal–support interactions in coprecipitated catalysts and multicomponent nanomaterials.



## INTRODUCTION

Nanometer-sized particles of metals and metal oxides can have unique catalytic, magnetic, and electronic properties that are often strongly dependent on their structural and chemical state. In catalytic reactions, for example, the activity for molecular turnovers, is well-known to depend on the type and abundance of surface sites on the nanoparticles.<sup>1–3</sup> Procedures for the synthesis of nanoparticles with well-defined shapes and surfaces are in principle available to address such structure-dependent properties.<sup>4–7</sup> However, during catalysis, the stability of nanoparticle morphology is not guaranteed.<sup>8–10</sup> Solid surfaces tend to restructure upon exposure to gas environments and nanoparticles therefore tend to dynamically adapt a shape and structure that is coupled to the reaction conditions. Hereby, new surface sites might be exposed and the catalytic functionality of the nanoparticle change.

Here we focus on the binary Cu/ZnO nanoparticle system which is relevant for the industrial synthesis of methanol<sup>11</sup> and has become a prototypical system for studying complex gas-dependent nanoparticle dynamics. Whereas Cu alone is active, the methanol production is significantly enhanced by the intimate contact with ZnO. The role of the Cu–ZnO interaction and the nature of the catalytic active surface site has been the subject of much research. Possible explanations for the Cu–ZnO synergy include gas-dependent morphology of

Cu<sup>12–16</sup> on ZnO, Zn-species segregation onto Cu,<sup>17</sup> Cu–Zn alloy formation,<sup>18–21</sup> and support-induced strain.<sup>22,23</sup> The relative importance of these different effects is still a subject of debate and could reflect the effect of the catalyst preparation and reaction conditions.<sup>20</sup>

Much information about the gas-dependent structure of Cu/ZnO-based methanol synthesis catalysts have been obtained using bulk X-ray or neutron characterization techniques.<sup>8,18</sup> In addition, adsorption techniques have been used to correlate the Cu surface area and methanol synthesis activity.<sup>24,25</sup> Despite these efforts there is still limited insight into the surface dynamics of the Cu/ZnO nanoparticle catalyst. For instance, recent studies of an industrial catalyst showed that under reducing conditions the copper area probed by reactive nitrous oxide frontal chromatography (N<sub>2</sub>O-RFC) is overestimated and that the overestimation originates from the presence of either metallic Zn in a CuZn surface alloy or from oxygen vacancies in ZnO.<sup>26,27</sup> Moreover, a spillover effect of hydrogen in the interface between Cu and ZnO has also been proposed to have a significant role in the synthesis of methanol.<sup>16,28</sup> Understanding such phenomena in more detail requires deeper

Received: October 3, 2014

Revised: December 8, 2014

Published: December 16, 2014

insight into the dynamic surface behavior of the Cu-ZnO nanoparticle system under reducing conditions. In order to address the dynamic surface behavior in the binary Cu and ZnO nanoparticle catalyst system, we have developed a new nanoparticle synthesis method invoking formation of mass-selected CuZn alloy nanoparticles and transformation of these into binary clusters of Cu and ZnO nanocrystals on a substrate. The binary Cu-ZnO nanoparticle clusters can be regarded as confined units of the industrial Cu/ZnO methanol catalyst,<sup>29–31</sup> and these simpler structures advantageously allow the structural and chemical state of the Cu-ZnO nanoparticle surface to be studied by complementary techniques such as X-ray photoelectron spectroscopy (XPS) and in situ transmission electron microscopy (TEM).

## RESULTS AND DISCUSSION

**Particle Synthesis.** The CuZn nanoparticles were produced in a cluster source<sup>32,33</sup> by gas aggregation of Cu and Zn sputtered off a solid target and subsequently mass selected by a quadrupole mass filter. First, the mass selected CuZn nanoclusters were deposited under ultra high vacuum (UHV) conditions ( $2 \times 10^{-10}$  mbar) onto a TiO<sub>2</sub> substrate (for XPS studies) or a carbon film supported on a Cu grid (for TEM studies). TEM images of the as-prepared particles showed an average diameter of  $7.7 \pm 1$  nm (Figure S1) for particles deposited with a mass filter setting of 6.5 nm. Next, the nanoparticles were exposed to oxygen in order to facilitate a phase separation into CuO and ZnO. Finally, an exposure to hydrogen was done in order to prepare well-defined nanoparticles of Cu and ZnO in intimate contact. The TEM samples were transferred through ambient air to the microscope and treated in situ therein, while the XPS samples were treated in a high pressure cell (HPC) attached to the UHV setup. During the oxidation treatment, the O<sub>2</sub> pressure was 1 mbar and 200 mbar for the TEM and XPS experiments, respectively. In the TEM, the temperature was 300 °C and, in the HPC, the temperature was 200 °C. The higher oxidation temperature in the TEM was necessary due to the lower obtainable O<sub>2</sub> pressure. In both cases the sample was oxidized for 1 h. During reduction, the H<sub>2</sub> pressure was 1 mbar for both experiments. In the TEM, the temperature was 300 °C, and in the HPC, the temperature was increased in steps of 1 h to a maximum of 250 °C.

For these three preparation steps (deposition, oxidation and reduction), Figure 1 shows the elemental surface composition as determined by XPS, which approximately probes the first 3–5 monolayers, depending on the electron energy. Further details on calculation of the composition are in the Materials and Methods section. In the as-deposited state, the line positions and shape of Cu L<sub>3</sub>VV and Zn L<sub>3</sub>M<sub>4,5</sub>M<sub>4,5</sub> reveal that the nanoparticles are metallic, and the 2p line intensities reveal an average composition of the nanoparticles of Cu:Zn ≈ 75:25. Due to the nature of the cluster source we anticipate a homogeneous mixture of Cu and Zn in the as-deposited nanoparticles. Hence the surface composition is expected to be representative for the bulk composition. Corresponding Auger spectra of Cu and Zn are shown in the following. The oxidation treatment of the nanoparticles results in a decrease of the apparent amount of Zn at the surface and the formation of CuO and ZnO with a composition of Cu:Zn ≈ 95:5. The satellite feature at 941 eV in the Cu 2p<sub>3/2</sub> line reveals that Cu is fully oxidized.<sup>34</sup> Moreover, the oxidation treatment results in a shift in the Zn Auger line revealing a transformation of Zn into

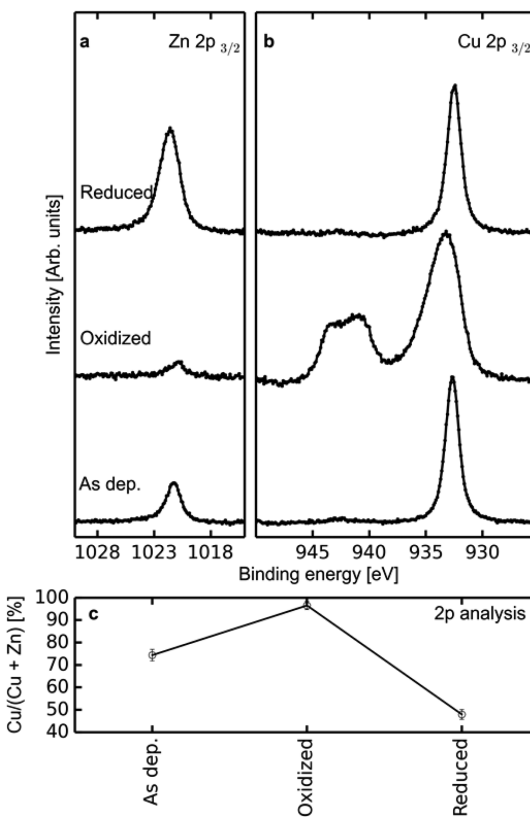


**Figure 1.** XPS Cu:Zn composition analysis. (a) Zn XPS 2p<sub>3/2</sub> in as-deposited, oxidized, and reduced condition. (b) Cu XPS 2p<sub>3/2</sub> in as-deposited, oxidized, and reduced condition. The 2p lines of Cu and Zn are background subtracted and normalized to the corresponding Cu spectrum. (c) The Cu:Zn composition taking sensitivity factors into account shown for the as-deposited, oxidized, and reduced condition, respectively.

ZnO. Finally, the reduction treatment of the oxidized nanoparticles reduces the CuO to Cu and changes the observed composition of Cu:Zn to ~45:55. The system thus does not revert to the as-deposited state upon reduction. The Cu/ZnO nanoparticles produced in this manner comprise our model for the methanol synthesis catalyst.

**Copper Oxidation State References.** In order to monitor the change of the oxidation state of copper in the phase separated state, the model system was exposed to reducing conditions (1 mbar H<sub>2</sub> in the HPC) at increasing temperatures, each temperature held for 1 h. After each reduction step, the sample was cooled to room temperature in the H<sub>2</sub> gas, the HPC was evacuated, and the sample was characterized by XPS under UHV conditions. Figure 2a shows normalized and background corrected XPS spectra at the Cu L<sub>3</sub>VV Auger line after each reduction treatment. In order to interpret these spectra, reference spectra were acquired of Cu, Cu<sub>2</sub>O, and CuO, with corresponding oxidation states Cu<sup>0</sup>, Cu<sup>I</sup>, and Cu<sup>II</sup>, respectively (Figure 2b). The metallic Cu reference spectrum was obtained by XPS measurement of the as-deposited nanoparticles. The copper oxide reference spectra were obtained by previously reported procedures.<sup>34</sup> To obtain the CuO reference spectrum, the as-deposited nanoparticles were fully oxidized by exposure to 200 mbar O<sub>2</sub> at 200 °C for 1 h in the HPC and subsequently measured by XPS. Finally, in order to obtain the partially oxidized Cu<sub>2</sub>O reference spectrum, the as-deposited sample was exposed to 200 mbar O<sub>2</sub> at room

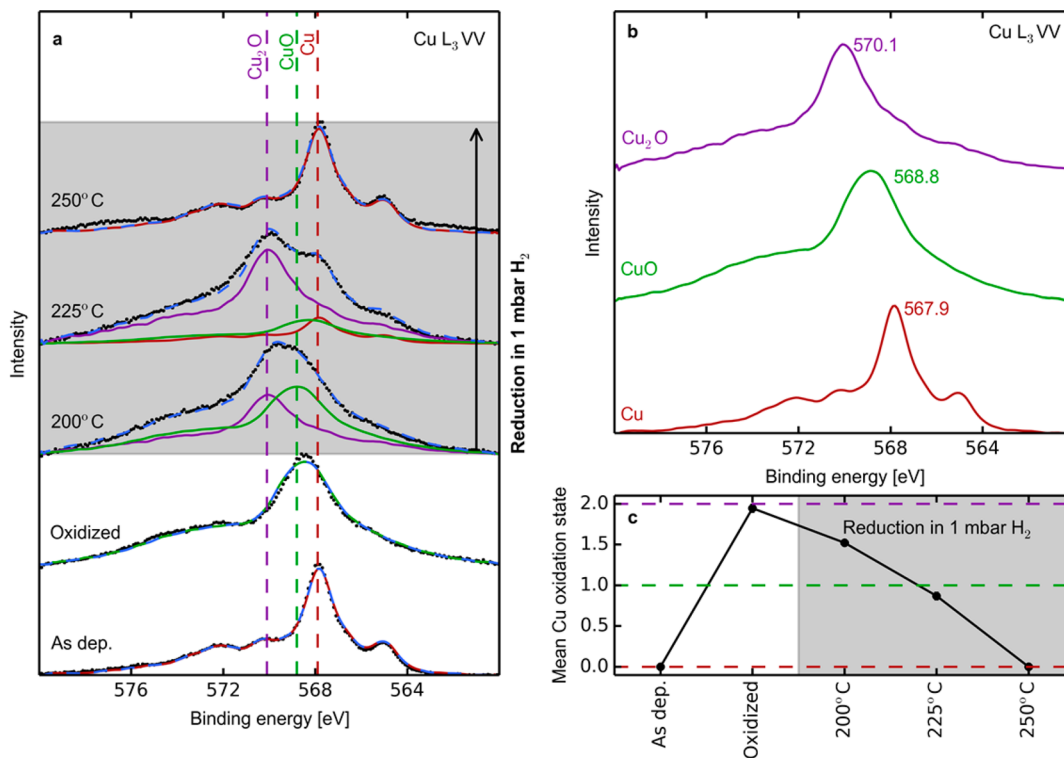


**Figure 2.** Changes to the XPS Cu L<sub>3</sub>VV features. (a) Reduction of CuZn nanoparticles in 1 mbar H<sub>2</sub>. Data points are shown as black dots while the light blue dashed lines are fits. The vertical lines indicate peak position for Cu (red), CuO (green), and Cu<sub>2</sub>O (purple). Subsequent to oxidation the nanoparticles are reduced in 1 mbar H<sub>2</sub> in steps for 1 h at increasing temperature. XPS is conducted in between each H<sub>2</sub> treatment. The change in the Cu L<sub>3</sub>VV Auger lines reveal that CuO is gradually reduced through the Cu<sub>2</sub>O state before it reaches full reduction at 250 °C. (b) The three different oxidation states of Cu. The fit in (a) is obtained by fitting a linear combination of the three Cu L<sub>3</sub>VV basis reference spectra. (c) The mean oxidation state of Cu as a function of reduction temperature. The mean oxidation state is obtained through the fits in (a).

temperature for 16 h in the HPC. For these three samples the Cu L<sub>3</sub>VV Auger lines are similar to spectra for Cu, CuO, and Cu<sub>2</sub>O as reported for copper thin films.<sup>34</sup> These spectra are therefore used as references in the following. Specifically, the different reference spectra consists of a main peak at 567.9, 568.8, and 570.1 eV for Cu, CuO, and Cu<sub>2</sub>O, respectively, corresponding, for the Al anode, to electron kinetic energies of 918.7, 918.8, and 916.5 eV.

A linear combination of the three references (Cu, CuO, and Cu<sub>2</sub>O) can be fitted to the Cu L<sub>3</sub>VV Auger lines in Figure 2a and the relative abundance of each phase is determined from the fitting parameters. The results in Figure 2a show that the as-deposited nanoparticles consist only of metallic Cu. As shown before, in the case of exposure to 200 mbar O<sub>2</sub> at 200 °C, the nanoparticles consist of copper in its fully oxidized state, i.e., CuO. During the reduction at successively higher temperatures, copper gradually transforms from fully oxidized CuO, through the Cu<sub>2</sub>O phase, to fully reduced Cu.

Furthermore, the fitting of the Cu L<sub>3</sub>VV Auger line into Cu<sup>0</sup>, Cu<sup>I</sup>, and Cu<sup>II</sup> allows for an estimation of the average copper oxidation state in the nanoparticles (Figure 2c). This procedure shows that copper in the oxidized CuZn nanoparticles is reducible under 1 mbar H<sub>2</sub> at 250 °C for 1 h. These conditions are similar to those used in the present in situ TEM experiments and consistent with previous in situ TEM studies.<sup>15,16,35</sup>

**In Situ TEM Imaging.** Next, the relationship between the oxidation state and the morphology of the nanoparticles is addressed by in situ TEM of the nanoparticles under exposure to 1 mbar of H<sub>2</sub> or O<sub>2</sub>. Figure 3a shows a frame-averaged TEM

image of a Cu/ZnO nanoparticle supported on carbon under exposure to 1 mbar H<sub>2</sub> at 300 °C. In order to interpret the TEM image, different crystal phases present in the nanoparticle are identified from the crystal lattice fringe spacings. Figure 3b shows a fast Fourier transform (FFT) revealing several different lattice spacings and directions. By masking out a given lattice spot in the FFT and inverting the FFT, the spatial location of the corresponding crystal phase is readily identified. For example, Figure 3c shows annular masks superimposed on the FFT in Figure 3b at reciprocal lattice vectors of 1/2.08 Å<sup>-1</sup> and 1/1.81 Å<sup>-1</sup>, corresponding to the (111) and (200) planes of Cu. The mask width is 1/0.03 Å<sup>-1</sup>. Figure 3d shows the corresponding inverted FFT revealing that metallic Cu comprises the large central region of the nanoparticle. Figures 3e,f show similarly an annular mask at lattice spacings of 2.81 and 2.60 Å, corresponding to the (010) and (002) planes of ZnO, and the corresponding inverted FFT of the ZnO location. This procedure was employed for the interpretation of the spatial location of the various crystalline phases depicted in the high-resolution TEM images. Specifically, the image analysis focuses on the four relevant phases of Cu, CuO, Cu<sub>2</sub>O, and ZnO which each has unique crystal plane distances as depicted by the colored annular masks superimposed in Figure 3g. Hereby, each crystal phase is characterized by its spatial domain in the TEM image and the superposition of all filtered crystal phases provides a fingerprint of the relative content and location of the different crystal phases as illustrated in Figure 3h.

**Reduction/Oxidation Cycles.** The ex situ XPS and the in situ TEM methods outlined above are used to monitor the

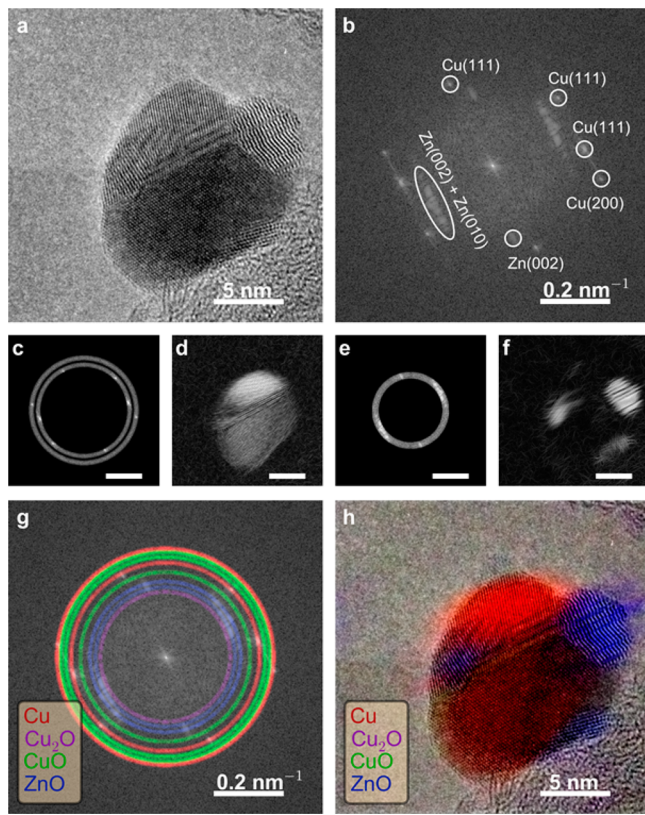


**Figure 3.** (a) TEM image of a Cu nanoparticle decorated with ZnO (1 mbar H<sub>2</sub>, 300 °C). (b) Fast Fourier Transform (FFT) shows crystal lattice vectors. (c) Annular masks applied to the FFT at 1/2.08 and 1/1.81 Å<sup>-1</sup>, corresponding to (111) and (200) planes of Cu. Mask width 1/0.03 Å<sup>-1</sup>. (d) Inverse FFT (IFFT) of (c). (e) Annular masks applied at lattice spacings of 1/2.81 and 1/2.60 Å<sup>-1</sup>, corresponding to (010) and (002) planes of ZnO. (f) IFFT of (e). (g) Annular masks superimposed on (b) for each unique lattice spacing of Cu, Cu<sub>2</sub>O, CuO, and ZnO (Table 1) with corresponding color code. (h) The image (a) with colored crystal phase domains superimposed.

CuZn nanoparticles during successive reduction and oxidation cycles. While XPS is a strong averaging technique providing a global picture of the surface composition and oxidation state of the entire ensemble of nanoparticles, TEM imaging is a strong local tool providing insight into the nonperiodic structural features of the nanoparticles, such as their shapes and surfaces that are needed to explain the global trends. The TEM images were acquired of as-deposited nanoparticles under high vacuum conditions and in situ during subsequent exposure to 1 mbar O<sub>2</sub> and H<sub>2</sub> at 300 °C, respectively (Figure 4a–d). The XPS data were acquired starting from an as-deposited sample treated first in 1 mbar O<sub>2</sub> and H<sub>2</sub>, as described above, and subsequently in 200 mbar O<sub>2</sub> or H<sub>2</sub> at 200 °C (Figure 4e). For the XPS experiments a higher gas pressure was used to ensure full reduction and oxidation (Figure 5). This pressure is, however, not possible to obtain in the applied microscope configuration. Figure 4 compiles the combination of in situ TEM and XPS data. When alternating between the oxidized state and the reduced state, the XPS analysis shows that the surface ratio between Cu and Zn changes reversibly, with the apparent amount of Cu varying from ~55% to ~85%. A change in surface composition of Cu and Zn has previously been reported by means of low-energy ion scattering experiments on Cu/ZnO/SiO<sub>2</sub>.<sup>36</sup>

One possible explanation for this reversible change in the surface of the nanoparticles is encapsulation and decapsulation of ZnO by CuO. Encapsulation leads to a hindrance of Zn 2p photoelectrons in reaching the analyzer, and decapsulation reestablishes the Zn signal, as observed. Figure 4a demonstrates a reduced CuZn nanoparticle consisting of separate domains of metallic Cu (red) and ZnO (blue). In Figure 4b, the nanoparticle is in the oxidized state with a CuO domain (green) extending across the entire nanoparticle and with a ZnO domain (blue) present only inside the projected image of the nanoparticle. As the TEM images represent two-dimensional projections, this observation is consistent with crystalline ZnO in the subsurface region of the nanoparticle. The finding agrees with the XPS data which shows that the Zn signal is drastically damped during these oxidizing conditions (Figure 4e). Upon rereduction, the TEM shows that the nanoparticle reverts back toward its original state. In Figure 4c, faint lattice fringes corresponding to crystalline ZnO (blue) and a core with darker contrast is observed. In the intermediate state between fully oxidized and fully reduced, shown in Figure 4c, the crystals are oriented such that no major zone axes are parallel with the incident electron beam, which results in a lack of clearly resolved atomic lattice fringes. This, in turn, has the consequence that the automatic coloring routine will not add color, and Figure 4c thus represents the original TEM image, except for the blue coloring of the faintly resolved ZnO. In Figure 4d, the darker core appears with lattice fringes and the fringe spacing corresponds to metallic Cu. Moreover, the ZnO nanocrystal reappears on the Cu surface close to the position as in the reduced state (Figure 4a). Thus, in the example shown in Figure 4d, the nanoparticle has reverted back close to its original configuration with ZnO sitting at the surface of the metallic Cu, which is also consistent with the XPS data in Figure 4e, showing that the ZnO content recovers almost reversibly upon rereduction. For Figure 4(a–d), the nanoparticle is deemed reduced or partly reduced/oxidized, based only on the observation of lattice spacings from Cu metal or from any Cu oxide. It cannot be excluded that smaller crystal domains, representing Cu oxide in the reduced state and Cu metal in the oxidized state of the nanoparticle, may be simultaneously present, because a tilted orientation of the crystal domain with respect to the electron beam direction could prevent their identification in the high-resolution TEM image. In fact, images obtained at different regions of the sample showed the presence of copper oxide after the 5 h reduction in 1 mbar H<sub>2</sub> at 300 °C. This difference could be due to temperature variations across the TEM grid or an accelerated reduction rate under electron illumination in Figure 4, and from the discussion below the difference is attributed to the former cause. The encapsulation/decapsulation mechanism can, however, be explained by considering the crystal structure of Cu and CuO. When the sample is oxidized, the copper phase content will expand and take up more space than of metallic copper. As the oxide grows it appears to cover the ZnO. This may happen due to the different diffusion rate of Cu and O in CuO.<sup>37</sup> Because Cu diffuses faster than O in CuO, the oxide tends to grow on the surface of the existing oxide, which may create voided particles, or, as in the present case, may lead to an encapsulation of the ZnO sitting on the Cu surface. No voided particles were observed in the present study. During reduction, the CuO will consequently shrink and start to reveal ZnO. A rough estimate of the particle volume based on the projected areas reveals volume conservation between Figure 4a and d.

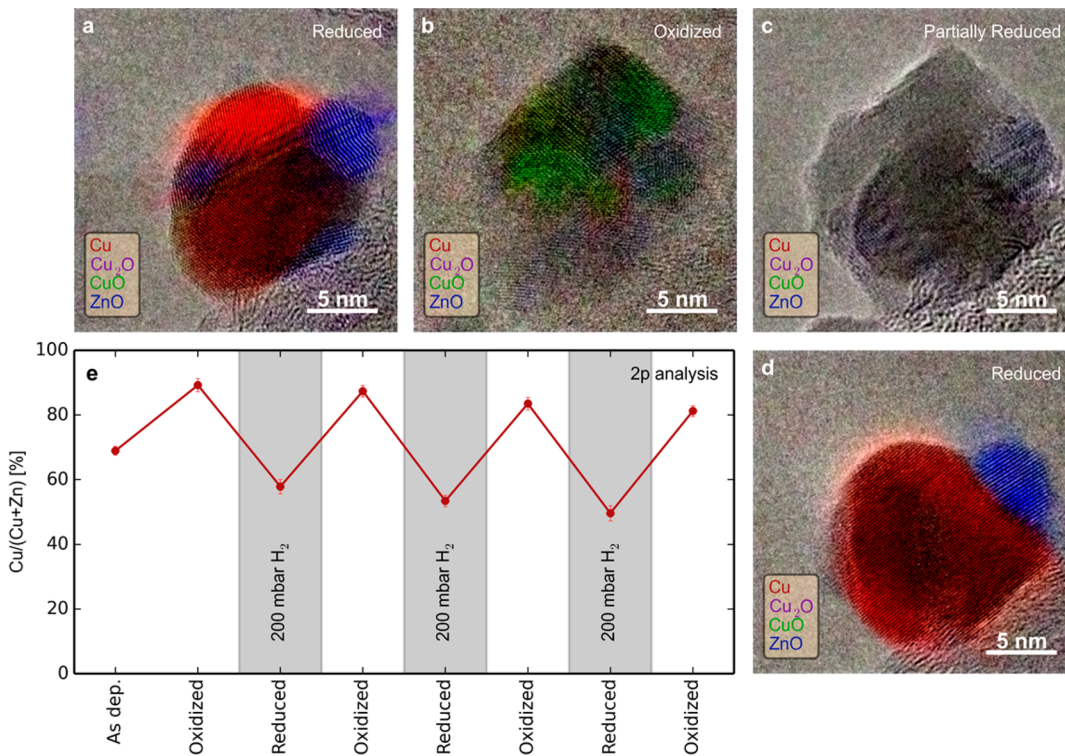


**Figure 4.** (a–d) In situ TEM images of the same CuZn nanoparticle during an oxidation/reduction cycle. (a) Reduced nanoparticle after 5 h in 1 mbar H<sub>2</sub> at 300 °C. (b) Oxidized nanoparticle after 1 h in 1 mbar O<sub>2</sub> at 300 °C. (c) Partly reduced nanoparticle after 0.5 h in 1 mbar H<sub>2</sub> at 300 °C. (d) Fully reduced particle after 1.5 h in 1 mbar H<sub>2</sub> at 300 °C. For (a–d), the nanoparticle is deemed reduced or partly reduced/oxidized based only on the observation of lattice spacings from Cu metal or from any Cu oxide. It can therefore not be excluded that small crystal domains, representing Cu oxide in the reduced state and Cu metal in the oxidized state, may be simultaneously present because a tilted orientation with respect to the electron beam could prevent their identification. (e) Ratio between the XPS signal from the Cu 2p<sub>3/2</sub> and Zn 2p<sub>3/2</sub> lines after oxidation (200 mbar O<sub>2</sub> for 1 h at 200 °C) and reduction (200 mbar H<sub>2</sub> for 1 h at 200 °C).

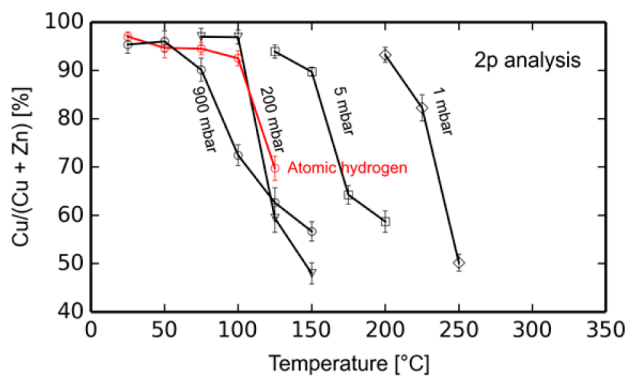


**Figure 5.** Change in ratio between the Cu 2p<sub>3/2</sub> and Zn 2p<sub>3/2</sub> XPS line as a function of increasing temperature in different pressures of hydrogen. At 1 mbar the Cu/(Cu + Zn) ratio drops when the temperature reaches 250 °C. This is the same conditions needed to fully reduce the Cu (Figure 2). The same behavior, although at lower temperature, is observed for 200 mbar H<sub>2</sub>, 900 mbar H<sub>2</sub> and atomic hydrogen at a pressure of 10<sup>-6</sup> mbar H<sub>2</sub>. In the latter case, the ratio changes at 125 °C. At 5 mbar H<sub>2</sub> the Cu/(Cu + Zn) ratio drops when the temperature reaches 175 °C.

The expansion from Figure 4a to b is 88%, reasonably close to the 72% increase, expected from the difference in unit cell volume between Cu and CuO. A similar analysis of 88 particles in the same area shows an average volume increase of 82% (Figure S2).

The single image series in Figure 4 reveals the transformation of the nanoparticle during the reduction–oxidation–reduction

cycle. Whereas the Cu nanocrystal and a ZnO nanocrystal apparently transforms reversibly, some smaller ZnO nanocrystals disappears and a single ZnO nanocrystal emerges on the left side of the particle. Because of the narrow size distribution of the nanoparticles and a presumably low spread of their composition, the observations in Figure 4 are likely to be representative for the deposited nanoparticles. Furthermore, the XPS data (Figure 4e) shows a slight decrease in the Cu:Zn ratio as repeated cycles are performed. This decrease in the Cu:Zn ratio for repeated cycles can be explained by migration of Cu between individual Cu/ZnO nanoparticles and is known to be a possible mechanism for Cu sintering in methanol synthesis catalysts.<sup>38</sup> In the present study sintering was observed during the reduction/oxidation cycle of the TEM sample (Figure S2). Coarsening of Cu particles lowers the Cu surface area of the sample, thus effectively also lowering the Cu:Zn ratio.

**Reduction of Cu in Different Environments.** Although the XPS and TEM experiments agree qualitatively, they differ by the gas pressure. To address this pressure gap, oxidized Cu-Zn nanoparticles are exposed to H<sub>2</sub> at different pressures and characterized by XPS. Prior to the reduction, the nanoparticles were oxidized by 200 mbar O<sub>2</sub>. The temperature required for reduction is presumably determined by either diffusion-limitations in the nanoparticles or limitations due to hydrogen dissociation. Thus, it is expected that the reduction temperature is lower at higher pressures because of the increased chemical potential of H<sub>2</sub>. Figure 5 shows the Cu:Zn composition obtained from the Cu 2p and Zn 2p line intensities as a

function of reduction temperature for five different reducing conditions.

First, the reduction of oxidized CuZn nanoparticles is addressed in 1 mbar H<sub>2</sub>. Figure 5 shows that the Cu:Zn ratio has a transition at 250 °C, which is the same temperature required to fully reduce CuO to Cu (see Figure 2). A similar sudden change in Cu:Zn ratio has been reported by Behrens et al. based on synchrotron XPS.<sup>18</sup> However, in their study the temperature for the transition occurs at a lower temperature and H<sub>2</sub> pressure (175 °C, 0.25 mbar). This will be further discussed below. The discrepancy in reduction temperature between the 1 mbar XPS (250 °C) and 1 mbar TEM (300 °C) in our experiments is attributed to an expected lower temperature away from the TEM Cu grid upon which the temperature is measured. The temperature at the nanoparticle site for our XPS and TEM investigations is therefore assumed similar.

Next, in 5 mbar H<sub>2</sub>, the transition occurs at 200 °C, lower than the 250 °C required for reduction in 1 mbar H<sub>2</sub>, indicating that reduction is hindered by the reductive potential of the H<sub>2</sub> gas. This tendency is followed upon reduction of the oxidized CuZn nanoparticles in 200 mbar H<sub>2</sub> for which the Cu:Zn ratio transition occurs already at 125 °C. In all cases the transition coincides with CuO reduction to Cu.

Finally, at 900 mbar reducing conditions, the curve shape is slightly different but the transition to a lower Cu content is below or similar to the 200 mbar experiment at 125 °C. This may indicate that for temperatures lower than 125 °C, oxygen diffusion from bulk to the surface in the CuO nanoparticle is kinetically hindered.

Another way of increasing the chemical potential for reduction is predissociation of H<sub>2</sub>.<sup>39</sup> The atomic hydrogen can be formed at UHV compatible pressures by ionization in a dedicated gas doser. Figure 5 shows that the predissociation is a very effective way of increasing the chemical potential of H<sub>2</sub> because the oxide-metal transition is observed at temperatures around 125 °C (see Figure S3 for detailed XPS data), similar to the 200 mbar H<sub>2</sub> conditions.

In the in situ TEM experiments, the reducing temperature of 300 °C was needed to fully reduce CuO in 1 mbar H<sub>2</sub> (as determined by inspection of high-resolution TEM images). This finding indicates that atomic hydrogen is not produced by the electron beam in significant amounts in the present experiments and suggests, in turn, that the variation in the degree of reduction across the TEM grid is rather due to temperature variations. Furthermore, the effect of the beam on creating atomic hydrogen might explain the temperature discrepancy with the results obtained on synchrotron XPS.<sup>18</sup>

**Reduction of ZnO.** To address the chemical state of zinc resulting from the reduction treatment, the Zn L<sub>3</sub>M<sub>4,5</sub>M<sub>4,5</sub> Auger line is considered in the following. Figure 6 evidently shows that the Zn in the as-deposited CuZn nanoparticles is metallic as the particles are deposited on the TiO<sub>2</sub> substrate.<sup>40,41</sup> After oxidation in 200 mbar O<sub>2</sub> at 200 °C, based on the comparison to literature,<sup>40</sup> Zn is present as ZnO as shown in Figure 6. Using these as-deposited and fully oxidized spectra as reference spectra for metallic and oxidized Zn, a linear combination can be fitted to the Zn L<sub>3</sub>M<sub>4,5</sub>M<sub>4,5</sub> Auger lines obtained after reduction in 1 mbar H<sub>2</sub> at different temperatures to determine the relative abundance of those species. At 250 °C, the Zn Auger line can best be fitted including a Zn-component resulting in the shoulder at 495 eV binding energy (991.6 eV kinetic energy). This indicates that

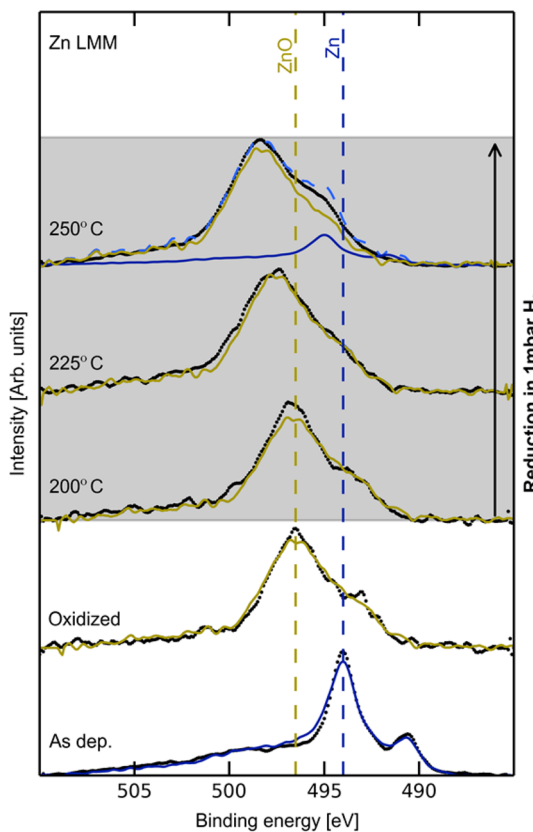


**Figure 6.** Zn L<sub>3</sub>M<sub>4,5</sub>M<sub>4,5</sub> Auger line obtained during the 1 mbar reduction experiment. Blue lines correspond to metallic Zn while yellow lines correspond to ZnO. The dotted black line is 7 point smoothed XPS data while the dashed light blue line is the best fit of the data based on the reference spectra of Zn and ZnO.

ZnO is partially reduced at this temperature. The presence of reduced Zn after low temperature reduction in H<sub>2</sub> has previously been reported<sup>26</sup> for a commercial catalyst. Moreover, it is observed that the Zn L<sub>3</sub>M<sub>4,5</sub>M<sub>4,5</sub> line shifts toward higher binding energies as the reduction temperature is increased. This effect may be related to charging effects in the TiO<sub>2</sub> substrate which is more pronounced at higher reductive potentials.<sup>42</sup> The separation between the ZnO and the Zn peak is kept fixed while performing the fitting routine.

The presence of reduced ZnO is observed at the same temperature needed to reduce CuO. The concurrent reduction for CuO and ZnO is also observed for reduction in 5 mbar H<sub>2</sub>, 200 mbar H<sub>2</sub>, 900 mbar H<sub>2</sub>, and in atomic hydrogen (see Figure S4 for the atomic hydrogen experiment). It is well-known that H<sub>2</sub> dissociates on Cu.<sup>43</sup> As ZnO is present at the surface of the nanoparticle during reduction of CuO (Figure 4), it is possible that ZnO reduction proceeds via spillover of dissociated hydrogen to sites at the ZnO surface from the reduced Cu.<sup>16,28</sup> Thus, it is likely that dissociated hydrogen can reduce ZnO to Zn at the interface between Cu and ZnO. The experiment shows that even at low pressures of hydrogen it is possible to reduce ZnO to Zn, coinciding with previous experiments made on a commercial catalyst.<sup>26</sup> However, a more pronounced Zn signal is observed in our experiments. We attribute this to the lower amount of ZnO in our model system compared to the commercial catalyst system, which increases the sensitivity for detection of metallic Zn. This stresses the advantage of using simplified model systems to investigate such complex systems.

## CONCLUSION

In order to address metal–support interactions in heterogeneous catalysis, a novel model approach is presented. It is demonstrated that size and composition selection of nanoparticles allows for generating a uniform ensemble of bimetallic nanoparticles and for combining spatial averaging and local techniques to probe gas-dependent dynamics in the nanoparticles. Specifically, the method is used to study the complex Cu-ZnO system representing the active part of industrial methanol synthesis catalysts. The as-prepared Cu–Zn particles were exposed to oxidizing and reducing atmospheres. By combining ex situ XPS and in situ TEM, it is observed that upon repeated oxidation-reduction cycles, the CuO tends to encapsulate and decapsulate the ZnO in a reversibly manner. Furthermore, the present findings reveal that the hydrogen reduction is sufficient to cause a reduction of the ZnO leaving metallic Zn in the surface. The metallic zinc is only observed as the copper is in the metallic states. On the basis of this, a spillover mechanism for the reduction of Zn has been proposed.

## MATERIALS AND METHODS

**Ultra High Vacuum Setup.** The cluster synthesis, spectroscopy experiments, and high pressure treatments were conducted in a home build multipurpose UHV chamber with a base pressure in the  $2 \times 10^{-10}$  mbar pressure range and capable of performing XPS measurements. Furthermore, it is possible to treat samples in a HPC annexed to the chamber. Finally, the UHV setup is in connection with a cluster source capable of producing metallic nanoparticles with a narrow size distribution in the range 3–10 nm, described elsewhere.<sup>33,44,45</sup> All transfers between different parts of the chamber are in UHV.

For this study, metallic CuZn nanoparticles are deposited on a TiO<sub>2</sub>(110) rutile single crystal. The nanoparticles are produced by a cluster source developed by Mantis Deposition Ltd. The mass filter of the cluster source was adjusted to select particles with a diameter of 9 nm. Based on earlier studies on the same cluster source, operated under similar conditions, the standard deviation of the size distribution of the nanoparticles is expected to be 2 nm.<sup>45</sup> The CuZn clusters are sputtered off a metal target with Cu:Zn composition of 90:10. The metal clusters are condensed in a cooled gas-aggregation zone and mass filtered by a quadrupole. After deposition of CuZn nanoparticles on the TiO<sub>2</sub>(110) substrate the nanoparticles were investigated by XPS. The Cu 2p<sub>3/2</sub> and Zn 2p<sub>3/2</sub> XPS lines reveal a 76:24 atomic composition in the surface region probed by the Al K $\alpha$  X-rays (1486.6 eV). Comparison of the Cu(L<sub>3</sub>VV) and Zn(L<sub>3</sub>M<sub>4,5</sub>M<sub>4,5</sub>) lines to literature confirms that the produced nanoparticles are metallic.<sup>34,40,41</sup> In order to bring the CuZn nanoparticles in a state similar to the commercial methanol catalyst, the sample is oxidized at 200 °C in 200 mbar O<sub>2</sub> for 1 h in the HPC by a molybdenum substrate heater. The Cu Auger and Zn Auger lines confirm that the probed region of the nanoparticle becomes fully oxidized. The ratio between the amount of Cu and Zn is determined by integrating the 2p<sub>3/2</sub> lines from each element, taking sensitivity factors into account. After phase separation of Cu and Zn, i.e., oxidation, two different set of experiments are performed; (1) a repeated cycle of reduction and oxidation at 200 °C and 200 mbar H<sub>2</sub> and O<sub>2</sub> respectively. The sample is exposed to the gas for 1 h. Between each gas treatment the sample is investigated by XPS. (2) A cumulative reduction of

the CuZn in 1 mbar H<sub>2</sub> at increasing temperatures, starting at 200 °C and ending at 250 °C, in steps of 25 °C. Each step was held for 1 h. XPS analysis of the sample is performed after each temperature step. The stepwise reduction experiment has also been conducted in 5 mbar H<sub>2</sub>, 200 mbar H<sub>2</sub>, 900 mbar H<sub>2</sub>, and in the presence of atomic hydrogen. The atomic hydrogen was produced by a hot filament with an emission current of 10 mA pointing in the direction of the sample in a background pressure of  $1 \times 10^{-6}$  mbar H<sub>2</sub>. In all XPS experiments, the presence of contaminates such as carbon has been checked for. In none of the experiments a peak at the C 1s relevant binding energy could be detected. A typical overview scan is presented in Figure S5. A Shirley background is applied to the XPS data during data treatment. Error bars are calculated by performing fits with 25 randomly chosen Shirley backgrounds. Presented data with no apparent error bar have errors smaller than the marker indicating the point.

**In Situ TEM.** In situ TEM was performed using a FEI Titan 80–300 environmental transmission electron microscope operated with primary electron energy of 300 keV.<sup>46</sup> Prior to the experiment, the image aberration corrector was tuned using a Au/C cross-grating (Ager S106) and the spherical aberration coefficient was set in the range of -10 to -20 μm.

Samples for in situ TEM were prepared by depositing CuZn alloy particles directly onto a lacey carbon film supported on a Cu TEM grid. Nanoparticles with a diameter of 6.5 nm were selected by tuning the filter of the cluster source. Based on TEM investigations this resulted in an average projected diameter of  $7.7 \pm 1$  nm (Figure S1). The difference between the mass filter setting and the TEM measurement is ascribed to particle wetting on the support and possible surface oxidation of the CuZn particles, both effects will increase the projected diameter. The cluster deposition was carried out under UHV conditions, and subsequently the sample was transferred in air to either a glovebox (the levels of oxygen and moisture were below 0.1 ppm and 1 ppm, respectively) or directly into the electron microscope. The air exposure amounted to maximum 30 min.

For the in situ experiments, a TEM grid was placed in a Gatan furnace type heating holder (model 628). The sample was exposed to 1 mbar O<sub>2</sub> (Air Liquide, nominel purity N4.5) or 1 mbar H<sub>2</sub> (CK gas, nominel purity N6.0). The TEM is conducted using low electron dose-rate and low electron dose conditions in order to suppress beam excitations and atom displacements in the gas-sample system and to ensure structures and processes inherent to the nanoparticle catalysts are detected.<sup>46,47</sup> The low electron doses compromise the image signal-to-noise ratio, and so, to detect features in the specimens at high resolution, signal enhancement is pursued in two steps. First, the projection system and charged-coupled device camera (Gatan US1000) was operated with an effective pixel size of 0.063 nm, which is sufficient for resolving the Cu (111) and (200) lattice spacing of 0.21 and 0.18 nm, respectively. Second, frame-averaging is pursued by acquisition of 20 consecutive frames (each with a CCD exposure time of 1 s), postalignment of the frames using cross correlation<sup>48</sup> in a Matlab script and, finally, summation of the aligned frames into the final image. All displayed images represent such a frame-average. Specifically, the TEM frames were acquired at an electron dose rate of  $300 \text{ e}^-/\text{\AA}^2 \text{ s}$  and an estimated total dose of  $90\,000 \text{ e}^-/\text{\AA}^2$  (ca. 5 min exposure) of a given sample area. Figure 4a–d represents images acquired of that particular particle with an accumulated electron dose of approximately 2.7

$\times 10^5$ ,  $7.2 \times 10^5$ ,  $8.1 \times 10^5$ , and  $9.0 \times 10^5$  e<sup>-</sup>/Å<sup>2</sup>. These imaging conditions were sufficiently low to avoid beam-induced artifacts as the comparison with the pressure-dependent XPS reduction data shows (Figure S). Several particles were imaged under reducing conditions, and the overall configuration of the reduced particle shown in Figure 3 (reduced Cu decorated with ZnO) is representative of the particles seen with *in situ* TEM in reducing atmosphere. Only the particle shown in Figure 4 was imaged with high magnification under both reducing and oxidizing conditions. 88 particles in the same area were imaged with low magnification under both reducing and oxidizing conditions (Figure S2).

Domains of crystalline Cu, CuO, Cu<sub>2</sub>O, and ZnO were identified in high-resolution TEM images using for each phase the unique lattice spacings as described in Table 1. Annular

**Table 1. Crystal Structures and Corresponding Lattice Planes (*hkl*)<sup>a</sup>**

crystal phase	( <i>hkl</i> )	d (Å)
CuO	(-202)	1.87
	(-112)	1.96
Cu <sub>2</sub> O	(011)	3.02
Cu	(200)	1.81
	(111)	2.08
ZnO	(002)	2.60
	(010)	2.81

<sup>a</sup>Crystal structures from ICSD.<sup>49</sup>.

masks in the FFT included a region of  $\pm 1/0.015$  Å<sup>-1</sup> centered on the corresponding lattice vector. Masking of the FFT employed an edge smoothing. The edge smoothing used a circular averaging filter with a size of 3 pixels. Color coding was implemented in a Matlab script.

## ■ ASSOCIATED CONTENT

### S Supporting Information

Overview XPS scan as well as details on reduction experiment in atomic hydrogen. This material is available free of charge via the Internet at <http://pubs.acs.org>.

## ■ AUTHOR INFORMATION

### Corresponding Authors

\*E-mail: sth@topsoe.dk.

\*E-mail: Jane@fysik.dtu.dk.

### Notes

The authors declare no competing financial interest.

## ■ ACKNOWLEDGMENTS

The authors gratefully acknowledge The Danish National Research Foundation's Center for Individual Nanoparticle Functionality, supported by the Danish National Research Foundation (DNRF54). The authors acknowledge S. B. Vendelbo for fruitful discussions regarding coloring of TEM images.

## ■ ABBREVIATIONS

UHV, ultra high vacuum; XPS, X-ray photoelectron spectroscopy; TEM, transmission electron microscopy

## ■ REFERENCES

- Li, Y.; Somorjai, G. A. Nanoscale Advances in Catalysis and Energy Applications. *Nano Lett.* **2010**, *10*, 2289–2295.
- Nørskov, J. K.; Bligaard, T.; Hvolbæk, B.; Abild-Pedersen, F.; Chorkendorff, I.; Christensen, C. H. The Nature of the Active Site in Heterogeneous Metal Catalysis. *Chem. Soc. Rev.* **2008**, *37*, 2163–2171.
- Bell, A. T. The Impact of Nanoscience on Heterogeneous Catalysis. *Science* **2003**, *299*, 1688–1691.
- Burda, C.; Chen, X.; Narayanan, R.; El-Sayed, M. A. Chemistry and Properties of Nanocrystals of Different Shapes. *Chem. Rev.* **2005**, *105*, 1025–1102.
- An, K.; Somorjai, G. A. Size and Shape Control of Metal Nanoparticles for Reaction Selectivity in Catalysis. *ChemCatChem* **2012**, *4*, 1512–1524.
- Xia, Y.; Xiong, Y.; Lim, B.; Skrabalak, S. E. Shape-Controlled Synthesis of Metal Nanocrystals: Simple Chemistry Meets Complex Physics? *Angew. Chem., Int. Ed.* **2009**, *48*, 60–103.
- Cuenya, B. R. Synthesis and Catalytic Properties of Metal Nanoparticles: Size, Shape, Support, Composition, and Oxidation State Effects. *Thin Solid Films* **2010**, *518*, 3127–3150.
- Topsoe, H. Developments in Operando Studies and in Situ Characterization of Heterogeneous Catalysts. *J. Catal.* **2003**, *216*, 155–164.
- Tao, F. F.; Salmeron, M. In Situ Studies of Chemistry and Structure of Materials in Reactive Environments. *Science* **2011**, *331*, 171–174.
- Porsgaard, S.; Merte, L. R.; Ono, L. K.; Behafarid, F.; Matos, J.; Helveg, S.; Salmeron, M.; Roldan Cuenya, B.; Besenbacher, F. Stability of Platinum Nanoparticles Supported on SiO<sub>2</sub>/Si(111): A High-Pressure X-Ray Photoelectron Spectroscopy Study. *ACS Nano* **2012**, *6*, 10743–10749.
- Hansen, J. B.; Nielsen, P. E. H. *Handbook of Heterogeneous Catalysis*; Ertl, G., Knözinger, H., Schuth, F., Weitkamp, J., Eds.; Wiley-VCH Verlag GmbH & Co. KGaA: Weinheim, Germany, 2008; pp 2920–2949.
- Clausen, B. S.; Schiøtz, J.; Gråbæk, L.; Ovesen, C. V.; Jacobsen, K. W.; Nørskov, J. K.; Topsoe, H. Wetting/ Non-Wetting Phenomena during Catalysis: Evidence from *In Situ* on-Line EXAFS Studies of Cu-Based Catalysts. *Top. Catal.* **1994**, *1*, 367–376.
- Ovesen, C. V.; Clausen, B. S.; Schiøtz, J.; Stoltze, P.; Topsøe, H.; Nørskov, J. K. Kinetic Implications of Dynamical Changes in Catalyst Morphology During Methanol Synthesis Over Cu/ZnO Catalysts. *J. Catal.* **1997**, *168*, 133–142.
- Grunwaldt, J.-D. D.; Molenbroek, A. . M.; Topsøe, N. Y.; Topsøe, H.; Clausen, B. S. In Situ Investigations of Structural Changes in Cu/ZnO Catalysts. *J. Catal.* **2000**, *194*, 452–460.
- Hansen, P. L.; Wagner, J. B.; Helveg, S.; Rostrup-Nielsen, J. R.; Clausen, B. S.; Topsøe, H. Atom-Resolved Imaging of Dynamic Shape Changes in Supported Copper Nanocrystals. *Science* **2002**, *295*, 2053–2055.
- Vesborg, P. C. K.; Chorkendorff, I.; Knudsen, I.; Balmes, O.; Nerlov, J.; Molenbroek, A. M.; Clausen, B. S.; Helveg, S. Transient Behavior of Cu/ZnO-Based Methanol Synthesis Catalysts. *J. Catal.* **2009**, *262*, 65–72.
- Viitanen, M. M.; Jansen, W. P. A.; Welzenis, R. G.; Van Brongersma, H. H.; Brands, D. S.; Poels, E. K.; Bliek, A. Cu/ZnO and Cu/ZnO/SiO<sub>2</sub> Catalysts Studied by Low-Energy Ion Scattering. *J. Phys. Chem. B* **1999**, *103*, 6025–6029.
- Behrens, M.; Studt, F.; Kasatkin, I.; Kühl, S.; Hävecker, M.; Abild-Pedersen, F.; Zander, S.; Girsdsies, F.; Kurr, P.; Kniep, B.-L.; et al. The Active Site of Methanol Synthesis Over Cu/ZnO/Al<sub>2</sub>O<sub>3</sub> Industrial Catalysts. *Science* **2012**, *336*, 893–897.
- Fujitani, T.; Nakamura, J. The Effect of ZnO in Methanol Synthesis Catalysts on Cu Dispersion and the Specific Activity. *Catal. Lett.* **1998**, *56*, 119–124.
- Topsoe, N.; Topsøe, H. On the Nature of Surface Structural Changes in Cu/ZnO Methanol Synthesis Catalysts. *Top. Catal.* **1999**, *8*, 267–270.

- (21) Naumann d'Alnoncourt, R. N.; Kurtz, M.; Wilmer, H.; Löffler, E.; Hagen, V.; Shen, J.; Muhler, M. The Influence of ZnO on the Differential Heat of Adsorption of CO on Cu Catalysts: A Microcalorimetric Study. *J. Catal.* **2003**, *220*, 249–253.
- (22) Günter, M. M.; Ressler, T.; Bems, B.; Büscher, C.; Genger, T.; Hinrichsen, O.; Muhler, M.; Schlögl, R. Implication of the Microstructure of Binary Cu/ZnO Catalysts for Their Catalytic Activity in Methanol Synthesis. *Catal. Lett.* **2001**, *71*, 37–44.
- (23) Kasatkin, I.; Kurr, P.; Kniep, B.; Trunschke, A.; Schlögl, R. Role of Lattice Strain and Defects in Copper Particles on the Activity of Cu/ZnO/Al<sub>2</sub>O<sub>3</sub> Catalysts for Methanol Synthesis. *Angew. Chem. Int. Ed.* **2007**, *119*, 7465–7468.
- (24) Chinchen, G. C.; Hay, C. M.; Vandervell, H. D.; Waugh, K. C. The Measurement of Copper Surface Areas by Reactive Frontal Chromatography. *J. Catal.* **1987**, *103*, 79–86.
- (25) Muhler, M.; Nielsen, L. P.; Törnqvist, E.; Clausen, B. S.; Topsøe, H. Temperature-Programmed Desorption of H<sub>2</sub> as a Tool to Determine Metal Surface Areas of Cu Catalysts. *Catal. Lett.* **1992**, *14*, 241–249.
- (26) Kuld, S.; Conradsen, C.; Moses, P. G.; Chorkendorff, I.; Sehested, J. Quantification of Zinc Atoms in a Surface Alloy on Copper in an Industrial-Type Methanol Synthesis Catalyst. *Angew. Chem., Int. Ed.* **2014**, *53*, 5941–5945.
- (27) Fichtl, M. B.; Schumann, J.; Kasatkin, I.; Jacobsen, N.; Behrens, M.; Schlögl, R.; Muhler, M.; Hinrichsen, O. Counting of Oxygen Defects Versus Metal Surface Sites in Methanol Synthesis Catalysts by Different Probe Molecules. *Angew. Chem., Int. Ed.* **2014**, *53*, 7043–7047.
- (28) Spencer, M. S. The Role of Zinc Oxide in Cu/ZnO Catalysts for Methanol Synthesis and the Water–gas Shift Reaction. *Top. Catal.* **1999**, *8*, 259–266.
- (29) Baltes, C.; Vukojevic, S.; Schuth, F. Correlations Between Synthesis, Precursor, and Catalyst Structure and Activity of a Large Set of CuO/ZnO/Al<sub>2</sub>O<sub>3</sub> Catalysts for Methanol Synthesis. *J. Catal.* **2008**, *258*, 334–344.
- (30) Behrens, M. Meso- and Nano-Structuring of Industrial Cu/ZnO/(Al<sub>2</sub>O<sub>3</sub>) Catalysts. *J. Catal.* **2009**, *267*, 24–29.
- (31) Słoczyński, J. Antisintering Criteria in the Metal—spacer Catalytic System. *Chem. Eng. Sci.* **1994**, *49*, 115–121.
- (32) Haberland, H.; Karrais, M.; Mall, M.; Thurner, T. Thin Films from Energetic Cluster Impact: A Feasibility Study. *J. Vac. Sci. Technol. A* **1992**, *10*, 3266.
- (33) Nielsen, R. M.; Murphy, S.; Strelle, C.; Johansson, M.; Chorkendorff, I.; Nielsen, J. H. The Morphology of Mass Selected Ruthenium Nanoparticles from a Magnetron-Sputter Gas-Aggregation Source. *J. Nanoparticle Res.* **2009**, *12*, 1249–1262.
- (34) Tahir, D.; Tougaard, S. Electronic and Optical Properties of Cu, CuO and Cu<sub>2</sub>O Studied by Electron Spectroscopy. *J. Phys.: Condens. Matter* **2012**, *24*, 175002.
- (35) Wagner, J. B.; Hansen, P. L.; Molenbroek, A. M.; Topsøe, H.; Clausen, B. S.; Helveg, S. In Situ Electron Energy Loss Spectroscopy Studies of Gas-Dependent Metal–Support Interactions in Cu/ZnO Catalysts. *J. Phys. Chem. B* **2003**, *107*, 7753–7758.
- (36) Jansen, W. P. A.; Beckers, J.; Heuvel, J. C. v. d.; Gon, A. W. D. v. d.; Bliek, A.; Brongersma, H. H. Dynamic Behavior of the Surface Structure of Cu/ZnO/SiO<sub>2</sub> Catalysts. *J. Catal.* **2002**, *210*, 229–236.
- (37) Nakamura, R.; Tokozakura, D.; Nakajima, H.; Lee, J.-G.; Mori, H. Hollow Oxide Formation by Oxidation of Al and Cu Nanoparticles. *J. Appl. Phys.* **2007**, *101*, 074303.
- (38) Rasmussen, D. B.; Janssens, T. V. W.; Temel, B.; Bligaard, T.; Hinnemann, B.; Helveg, S.; Sehested, J. The Energies of Formation and Mobilities of Cu Surface Species on Cu and ZnO in Methanol and Water Gas Shift Atmospheres Studied by DFT. *J. Catal.* **2012**, *293*, 205–214.
- (39) Helveg, S.; Lauritsen, J.; Lægsgaard, E.; Stensgaard, I.; Nørskov, J.; Clausen, B.; Topsøe, H.; Besenbacher, F. Atomic-Scale Structure of Single-Layer MoS<sub>2</sub> Nanoclusters. *Phys. Rev. Lett.* **2000**, *84*, 951–954.
- (40) Fu, S. S.; Somorjai, G. A. Zinc Oxide and Oxygen Overlayers on Cu(110): A Model for CuZnO Catalysts. *Appl. Surf. Sci.* **1991**, *48–49*, 93–103.
- (41) Kowalczyk, S.; Pollak, R.; McFeely, F.; Ley, L.; Shirley, D. L<sub>2,3</sub>M<sub>45</sub>M<sub>45</sub> Auger Spectra of Metallic Copper and Zinc: Theory and Experiment. *Phys. Rev. B* **1973**, *8*, 2387–2391.
- (42) Diebold, U. The Surface Science of Titanium Dioxide. *Surf. Sci. Rep.* **2003**, *48*, 53–229.
- (43) Michelsen, H. A.; Auerbach, D. J. A Critical Examination of Data on the Dissociative Adsorption and Associative Desorption of Hydrogen at Copper Surfaces. *J. Chem. Phys.* **1991**, *94*, 7502.
- (44) Nielsen, R. M.; Murphy, S.; Strelle, C.; Johansson, M.; Nielsen, J. H.; Chorkendorff, I. A Comparative STM Study of Ru Nanoparticles Deposited on HOPG by Mass-Selected Gas Aggregation Versus Thermal Evaporation. *Surf. Sci.* **2009**, *603*, 3420–3430.
- (45) Murphy, S.; Nielsen, R. M.; Strelle, C. E.; Johansson, M.; Nielsen, J. H. Catalytic Oxidation of Graphite by Mass-Selected Ruthenium Nanoparticles. *Carbon* **2011**, *49*, 376–385.
- (46) Jinschek, J. R.; Helveg, S. Image Resolution and Sensitivity in an Environmental Transmission Electron Microscope. *Micron* **2012**, *43*, 1156–1168.
- (47) Kisielowski, C.; Wang, L.-W.; Specht, P.; Calderon, H. A.; Barton, B.; Jiang, B.; Kang, J. H.; Cieslinski, R. Real-Time Sub-Ångstrom Imaging of Reversible and Irreversible Conformations in Rhodium Catalysts and Graphene. *Phys. Rev. B* **2013**, *88*, 024305.
- (48) Russ, J. C. *The Image Processing Handbook*, 6th ed.; CRC Press: Boca Raton, FL, 2011; p 885.
- (49) Fiz. Inorganic crystal structure database ICSD <http://icsd.fiz-karlsruhe.de>; accessed May 20, 2014.